Temperature-Dependent Anharmonic Phonons in Quantum Paraelectric KTaO₃ by First Principles and Machine-Learned Force Fields

Luigi Ranalli, Carla Verdi, Lorenzo Monacelli, Georg Kresse, Matteo Calandra, and Cesare Franchini*

Understanding collective phenomena in quantum materials from first principles is a promising route toward engineering materials properties and designing new functionalities. This work examines the quantum paraelectric state, an elusive state of matter characterized by the smooth saturation of the ferroelectric instability at low temperature due to quantum fluctuations associated with anharmonic phonon effects. The temperature-dependent evolution of the soft ferroelectric phonon mode in the quantum paraelectric KTaO₃ in the range 0–300 K is modeled by combining density functional theory (DFT) calculations with the stochastic self-consistent harmonic approximation assisted by an on-the-fly machine-learned force field. The calculated data show that including anharmonic terms is essential to stabilize the spurious imaginary ferroelectric phonon predicted by DFT in the harmonic approximation, in agreement with experiments. Augmenting the DFT workflow with machine-learned force fields allows for efficient stochastic sampling of the configuration space using large supercells in a wide temperature range, inaccessible to conventional ab initio protocols. This work proposes a robust computational workflow capable of accounting for collective behaviors involving different degrees of freedom and occurring at large time/length scales, paving the way for precise modeling and control of quantum effects in materials.

1. Introduction

The quantum paraelectric phase is an eminent example of a quantum state of matter. It is manifested by the suppression of the ferroelectric transition at low temperatures due to quantum fluctuations, as observed in strontium titanate (SrTiO₃, STO) and potassium tantalate (KTaO₃, KTO).[1] In these materials, the frequency of the polar transverse optical (TO) soft phonon mode does not turn unstable with decreasing temperature, as it occurs in regular ferroelectric materials such as BaTiO₃, but rather saturates and never reaches the zero frequency limit.[2,3] This behavior is associated with an unusual temperature dependence of the inverse dielectric constant at low temperature, at odds with the classical Curie–Weiss law[4–6] (see **Figure 1**a). Quantum paraelectric STO and KTO, lying on the border of the ferroelectric phase in the vicinity of the so-called quantum critical point (QCP),[6,7] can be driven toward the ferroelectric region by applying minuscule external perturbations such as strain,[8] hydrostatic pressure,[9,10] or isotopic substitution[11] (see Figure 1b). For this reason, STO and KTO are also named incipient ferroelectrics. How the transition occurs (i.e., how the long-wavelength $\mathbf{q}=0$ ferroelectric TO phonon mode ω_{FE} becomes stable) is a complex matter challenging to decipher.[12] However, there is a certain consensus on the importance of the anharmonic coupling between ω_{FE} and the low-T quantum lattice oscillations in determining the stabilization of ω_{FE} at helium temperatures in quantum

L. Ranalli, C. Verdi, G. Kresse, C. Franchini
Faculty of Physics and Center for Computational Materials Science
University of Vienna
Kolingasse 14-16, 1090 Vienna, Austria
E-mail: cesare.franchini@univie.ac.at

L. Ranalli
Vienna Doctoral School in Physics
University of Vienna
Boltzmanngasse 5, 1090 Vienna, Austria

L. Monacelli
"Sapienza" Dipartimento di Fisica
University of Rome
Piazzale Aldo Moro 5, 00185 Rome, Italy

M. Calandra
Department of Physics
University of Trento
Via Sommarive 14, I-38123 Povo, Italy

C. Franchini
Department of Physics and Astronomy "Augusto Righi"
Alma Mater Studiorum - Università di Bologna
40127 Bologna Italy

**ADVANCED
SCIENCE NEWS**

www.advancedsciencenews.com

**ADVANCED
QUANTUM
TECHNOLOGIES**

www.advquantumtech.com
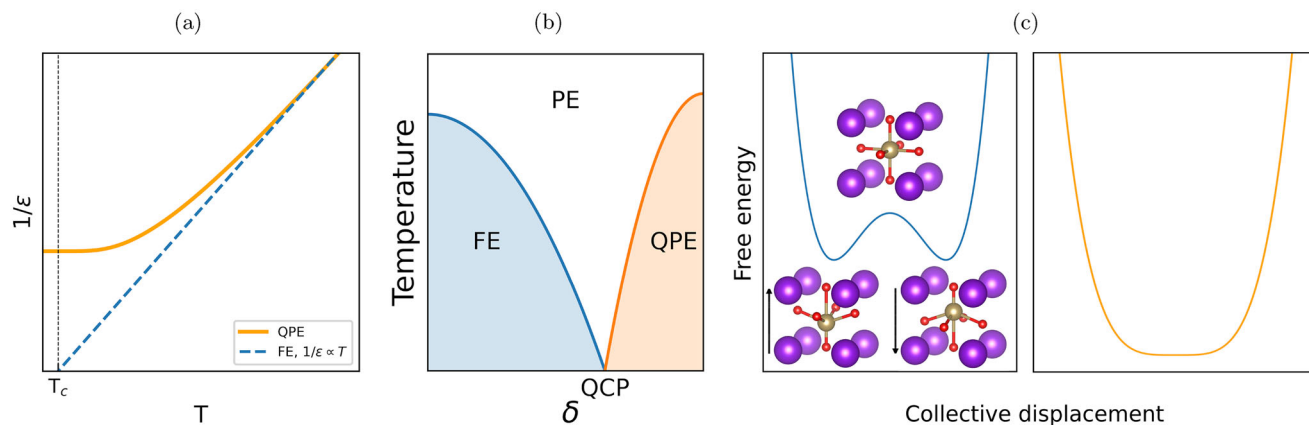
Figure 1. a) Schematic trend of the inverse dielectric constant as a function of temperature in the ferroelectric (FE) and quantum paraelectric (QPE) phase. In the FE phase, $1/\epsilon$ follows the characteristic linear behavior (dashed blue line) leading to a divergence of ϵ at a critical temperature T_c where the FE transition occurs. In a quantum paraelectric (orange solid line), in the proximity of T_c, the onset of quantum anharmonicity breaks down the linear regime establishing the QPE state. b) Qualitative phase diagram of the crossover between the FE and QPE phases as a function of a quantum tuning parameter δ; above a certain critical temperature, marked by the thick lines, the system lies in the paraelectric region. At 0 K, variations of the quantum tuning parameter (due, for example, to strain, hydrostatic pressure, or isotopic substitution) drive the FE-to-QPE transition across the so-called quantum critical point (QCP). c) Quantum free energy as a function of a collective atomic displacement in ferroelectric (left) and quantum paraelectric (right) systems. On the left, the quantum free energy as a function of the collective displacement amplitude induced by the unstable optical FE mode is here shown for a perovskite ABO_6 crystal. The soft FE phonon induces a FE displacement of the BO_6 octahedron (insets) which lowers the quantum free energy forming the typical double-well profile. In a QPE regime (right), the FE transition is inhibited due to quantum fluctuations and phonon anharmonicity. The inclusion of the anharmonic self-energy contributions at 0 K in the SSCHA calculations flatten the free energy removing the FE minima and establishing the QPE state.

paraelectrics.[13–15] Within the Landau model of displacive phase transitions, the quantum paraelectric (QPE) state can be viewed as the crossover between the ferroelectric (FE) state, characterized by the typical double-well energy surface, and the standard parabolic paraelectric (PE) behavior, resulting in quartic contributions[16] that flatten the free energy curve (Figure 1c). In QPE materials, quantum fluctuations and anharmonic effects at low temperature stabilize the QPE solution that becomes the genuine (and highly perturbable) ground state of the system.
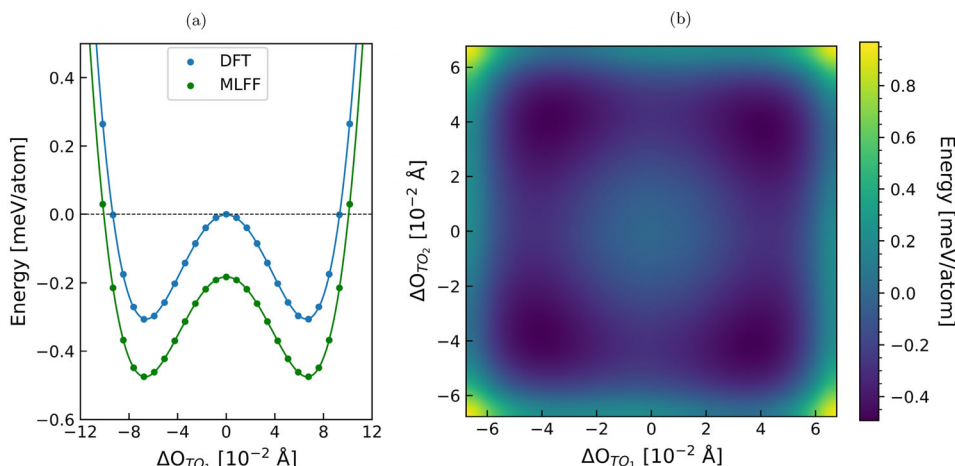
Abundant experimental data on the temperature decrease of the long-wavelength FE phonon and dielectric response in STO and KTO are available in literature.[6,17] The measurements have been rationalized by various phenomenological models either based on extensions of the classic description of Slater,[18] such as the Barrett[13] and Vendik[19] models,[5] or inspired by the Ginzburg–Landau–Wilson model such as the ϕ^4-quantum field model.[20,21] From a computational modeling perspective, path-integral Monte Carlo calculations using model Hamiltonians have provided essential insights into the role of quantum fluctuations and non-linear response function on the suppression of the ferroelectric transition.[22–24] Obtaining a microscopic description of the FE soft mode and the associated low-temperature non-linear behavior of the dielectric susceptibility is challenging. Recently, valuable efforts to address this complex issue from first principles have been reported.[25]

In this work, we design an efficient protocol to compute the temperature-dependent frequency $\omega_{FE}(T)$ of the characteristic soft phonon mode and associated dielectric response from first principles with full quantum and anharmonic effects. We select KTO as case material since it retains the ideal cubic perovskite structure over a wide temperature range down to the paraelectric phase and is not subjected to possible complica-

tions associated with structural phase transitions (as is the case in STO). To include ionic quantum and thermal fluctuations, we adopt the stochastic self-consistent harmonic approximation (SSCHA),[26,27] integrated with an on-the-fly machine learned force field (MLFF) scheme[28] for an efficient and accelerated exploration of the stochastic space.

Unlike alternative approaches such as extracting effective force constants from ab initio molecular dynamics (MD) trajectories,[29] the SSCHA method is based on a rigorous variational method involving the quantum free energy functional that directly yields the anharmonic free energy from a suitably parametrized harmonic Hamiltonian.[27,30–33] To evaluate the necessary partial derivatives of the free energy of the auxiliary harmonic system, the SSCHA method adopts a stochastic Monte Carlo (MC) procedure on a set of random ionic configurations generated in a chosen supercell following a Gaussian probability distribution. After the free energy functional minimization, the renormalized phonon frequencies are obtained along with other quantities such as the anharmonic phonon spectral functions and the anharmonic frequency linewidths.

The stochastic MC sampling is the most time-consuming part of the SSCHA workflow, as it requires the ground-state energy and interatomic forces for numerous supercell structures (of the order of a few thousands) obtained by randomly displacing the ions of the ideal crystal. To alleviate this huge computational cost, a reweighting technique is introduced (importance sampling) that allows for the simultaneous execution of several minimization steps with the same ensemble, with the price of a statistical degradation. Despite this speed-up, the computational cost of reaching well-converged results easily becomes prohibitive for systems requiring large supercells, posing a limit for large-scale samplings.

**ADVANCED
SCIENCE NEWS**

www.advancedsciencenews.com

**ADVANCED
QUANTUM
TECHNOLOGIES**

www.advquantumtech.com

Figure 2. Calculated ferroelectric instability. a) Electronic ground state energy as a function of the O displacement from the equilibrium position along the TO_1 unstable soft mode. The saddle point in the DFT calculation corresponds to the ideal cubic structure and represents the reference zero. The MLFF prediction is in very good agreement with the ab initio results. b) MLFF prediction of the 2D energy landscape as a function of the displacements involved in both the TO_1 and TO_2 degenerate modes. Calculations performed on a 3×3×3 supercell.

Machine learning algorithms have proved to be capable of efficiently accelerating computer simulations and represent an attractive way to cope with this technical limitation, enabling efficient speed-up and preserving accuracy.[36–38] Here, we accelerate the evaluation of SSCHA stochastic averages using a MLFF. The force field potential is trained on the fly during MD runs at different temperatures and is then employed to feed the inputs required by the MC integrals, thus reducing the computational cost of anharmonic phonon calculations by orders of magnitude.

2. Results

2.1. Harmonic Solution

We begin by assessing the quality of our MLFF by inspecting the ground-state energy as a function of the FE displacement as compared to direct DFT calculations (details about the MLFF training are reported in Section 3). The results are shown in **Figure 2**a. As expected, in the harmonic approximation, DFT predicts the cubic structure to be a saddle point that is meta-stable against opposite polar displacements of the O and Ta ions within the TaO_2 plane, as depicted in the inset of Figure 1c. This result is due to the neglect of anharmonic effects associated with the O-Ta-O polar vibration, as discussed in the next section. More precisely, this instability is controlled by two degenerate modes at Γ, TO_1 and TO_2: The TO_1 soft mode represents a motion along the crystallographic x-axis, and it is symmetry equivalent to the displacement along the z-axis described by TO_2.

The double well energy profile in Figure 2a shows that the displacive nature of the spurious ferroelectric phase transition in $KTaO_3$ is very well captured by MLFF both qualitatively and quantitatively. The DFT energy barrier amounts to −0.306 meV/atom at an O displacement of 0.059 Å in the TO_1 direction, whereas the MLFF predicts −0.293 meV/atom at 0.068 Å.

Since the TO_1 and TO_2 modes are degenerate, each linear combination of their associated eigenvectors is a legitimate solution of the problem for the non-ferroelectric phase. This is shown in Figure 2b, which reports the 2D map of the ground-state energy
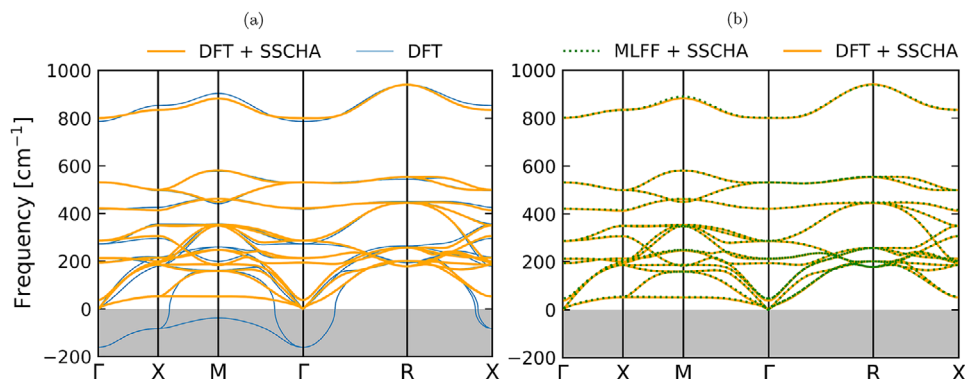
due to the combined action of both FE modes as obtained from the MLFF. This 2D map indicates a fourfold degenerate minimum at −0.493 meV/atom with respect to the saddle point located at (0,0).

2.2. Anharmonicity

Having tested the accuracy of the MLFF in accounting for the energy versus displacement profile, we now address its accuracy in obtaining the free energy Hessian with respect to the atomic positions, from which one can extract the anharmonic contributions to the phonon frequencies. The occurrence of a ferroelectric transition as a function of temperature can be detected by tracing the eigenvalues of the free energy Hessian divided by the square root of the mass matrix (the so called positional free energy Hessian; see Equation (51) in ref. [27]). An imaginary eigenvalue of the positional free energy diagnoses a ferroelectric transition.

In **Figure 3**a, we show the anharmonic phonon dispersions obtained from the eigenvalues of the positional free energy Hessian within the SSCHA at $T = 0$ K by using DFT on a 2×2×2 supercell and by including the self-energy correction in the free energy Hessian.[27] The phonon self energy is treated using the Bubble approximation that accounts for the most relevant three-phonon scattering processes. The result is compared with the DFT harmonic phonon dispersion. Not surprisingly, and in agreement with Figure 2a, the lowest energy optical phonon mode (the degenerate ferroelectric modes, labeled TO_1 and TO_2) at Γ is unstable in a large portion of the Brillouin zone, in disagreement with experimental data.[17] When quantum anharmonicity is switched on in the SSCHA method, the 0 K FE instability is removed. Remarkably, all other phonon modes are practically unaffected by the anharmonic correction. The calculated eigenvalue of the positional free energy for the TO_1 mode at Γ is 38.11 cm^{-1}. The contribution of the bubble term to the converged self-consistent dynamical matrix is −40.26 cm^{-1}.

We now proceed to integrate on-the-fly MLFF with SSCHA in order to accelerate the calculation of the phonon renormalization

2200131 (3 of 7)

ADVANCED
SCIENCE NEWS
www.advancedsciencenews.com

ADVANCED
QUANTUM
TECHNOLOGIES
www.advquantumtech.com

Figure 3. Calculated 0 K harmonic and anharmonic phonon dispersion. a) In DFT (blue lines), the harmonic phonon dispersion exhibits unstable FE TO_1 and TO_2 degenerate phonon modes at Γ. Within DFT+SSCHA (solid orange lines), the inclusion of the bubble term (anharmonic effects) renormalizes the unstable modes, while keeping the other branches unaffected. b) Comparison between DFT+SSCHA and MLFF+SSCHA (green dotted lines) anharmonic phonon spectra. Calculations performed on a 2×2×2 supercell.

and improve the stochastic sampling of the configuration space. The structure and technical details of the proposed protocol are described in Section 3. The results are shown in Figure 3b, which displays the comparison between the calculated DFT+SSCHA phonon dispersion along with the MLFF+SSCHA data. Note that for this specific comparison, here we employ an MLFF trained on a small 2×2×2 supercell, that is, the same supercell size adopted for the DFT+SSCHA calculations. For finite-temperature properties, we have employed a larger 3×3×3 supercell and a MLFF trained on large supercells as detailed in Section 3. The agreement is excellent in all regions of the phonon spectrum, including the TO_1 Γ-point frequency of 46.57 cm^{-1} and the −37.15 cm^{-1} bubble correction, very close to the corresponding DFT+SSCHA estimate. The neutron data at 20 K deliver a quite low frequency at Γ of 24.92 cm^{-1},[17] in line with our static dispersion data.

As the next level of complexity, we turn on finite temperature effects, which represent a key aspect to describe temperature-driven phase transitions and a huge obstacle for first principles approaches. Investigating the soft mode temperature behavior using ab initio calculations in SSCHA is computationally prohibitive, due to the large number of supercells required to achieve well-converged results for many temperatures. To obtain accurate results, we adopt a 3×3×3 supercell, with the corresponding MLFF trained to sample the configuration space up to 700 K. This yields a higher frequency of 59.63 cm^{-1} for the bubble-term corrected soft mode compared to the 46.57 cm^{-1} for the 2×2×2 case. Furthermore, the antagonistic bubble self-energy brings a lower correction of −11.24 cm^{-1} to the SSCHA virtual phonons. We note that the bubble term correction on top of the converged dynamical matrix returns a negative shift of the soft mode of 15.49 cm^{-1} at 300 K; hence, its contribution is almost temperature independent.

The soft mode temperature behavior predicted using the MLFF is plotted in **Figure 4**a, aligned with the low-T experimental data taken from ref. [39]. The MLFF predictions reproduce the measured trend quite well and show how the efficient integration of electronic structure methods, stochastic approaches, and machine learning provides a powerful computational framework that gives us the tools to explore regimes that were previously difficult to access.
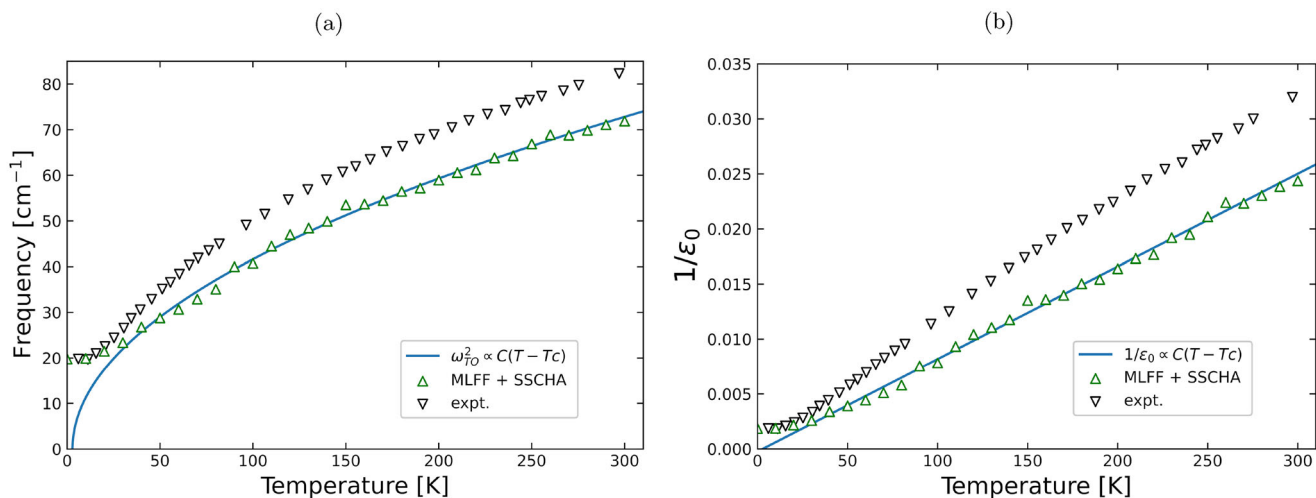
In particular, our data correctly predict the plateau below 30 K, in line with the expected theoretical trend collected in Figure 1a, proving the ability to capture the crucial role played by anharmonic effects in setting up the the quantum paraelectric state. By assuming the Lydanne–Sachs–Teller (LST) relation[40] $\frac{\omega_{LO}^2}{\omega_{TO}^2} = \frac{\epsilon_0}{\epsilon_\infty}$ connecting the optical phonon frequencies to the static and high frequency (above the phonon frequencies, but below any electronic energy scale) dielectric constants, and considering only the temperature dependence of the dielectric constant due to the TO dependence, we plot in Figure 4b the inverse of the dielectric constant $1/\epsilon_0$ as a function of temperature, together with the one extracted from the experimental data. The computed values of 4.635 and 212.68 cm^{-1} were adopted, respectively, for ϵ_∞ and the longitudinal optical mode ω_{LO}. A square-root fit of the frequency data, or equivalently a linear fit of the temperature-dependent inverse dielectric constant, clearly shows how the classic regime breaks down below 30 K, where the quantum nuclear motion coupled with anharmonicity becomes relevant.

We conclude by computing the phonon spectral function, which accounts for dynamical effects not included in the phonon spectra shown in Figure 3 and whose peaks give the phonon quasi-particles measured in inelastic neutron scattering. In **Figure 5**a,b, the phonon spectral function at 0 K and 300 K for a 3×3×3 supercell is plotted along the high-symmetry k-path and compared with available experimental data[17] and corresponding static dispersions. We note that the maxima of the spectral function coincide with the static dispersions (relative to the same 3×3×3 supercell) at both selected temperatures. In this case, the dynamical Bubble correction does not offer any substantial change on the static one, such as the appearance of satellite excitations. The agreement with the measured data is very good, even though the soft TO mode is overestimated by a few tens of cm^{-1} as pointed out above.

3. Computational Methods

The calculations were performed integrating the Vienna Ab initio Simulation Package (VASP)[41,42] with the stochastic self-consistent harmonic approximation (SSCHA) method[26,27] and

**ADVANCED
SCIENCE NEWS**

www.advancedsciencenews.com

**ADVANCED
QUANTUM
TECHNOLOGIES**

www.advquantumtech.com

Figure 4. Temperature evolution of the TO_1 Γ-point frequency (a) and of the inverse of the dielectric constant (b). In (a), inelastic neutron scattering measurements[39] (black empty triangles) and MLFF+SSCHA calculations with the inclusion of the bubble term are shown. The computed frequencies are shifted down by 34.71 cm^{-1} in order to match the experimental low-temperature soft mode frequency, to better appreciate the character of the frequency plateaus. A square-root fit (blue line) shows the breakdown of the paraelectric regime below 30 K and the onset of the quantum effects coupled with lattice anharmonicity, leading to a frequency plateau near 0 K. Analogously, the blue line in (b) shows the expected classical Curie–Weiss behaviour (see text) of the dielectric constant, calculated from the shifted frequencies of (a). Calculations performed on a 3×3×3 supercell.
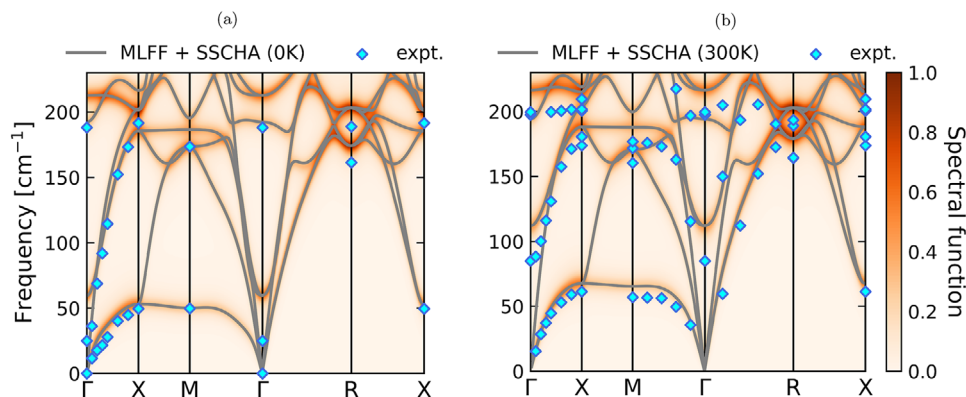
Figure 5. Color plot of the normalized phonon spectral function along the high symmetry path at a) 0 K and b) 300 K. In both cases, the maxima of the spectral function in darker red coincide with the static dispersion (full lines). The results are compared with the experimental data at 20 and 296 K[17] (diamonds). Calculations performed on a 3×3×3 supercell.

the phonon package Phonopy.[43] All DFT calculations were executed at the meta-GGA level using the Strongly Constrained and Appropriately Normed (SCAN) functional[44] and projector augmented wave (PAW) potentials,[45] using a plane-wave cutoff of 800eV. For this purpose, a computational workflow was constructed, including a VASP-to-SSCHA interface and the use of a MLFF in computing energies and forces associated with the generated ensembles within the SSCHA framework. The workflow is schematically depicted in **Figure 6** and consists of the following parts:

1. Construction of the trial harmonic dynamical matrix built on a cubic unit cell of $KTaO_3$ at the experimental lattice constant of 3.9842 Å.[15]
2. Ensembles generation and self-consistent SSCHA loop. The free energy minimization was executed through a force con-

stant gradient descent, keeping the atomic positions and volume fixed. Around 15 000 ensembles were needed in the self-consistency loop at 0 K (the last 5000 ensembles were also employed at the end of it for computing the bubble correction).

3. Speed-up of the stochastic MC sampling by means of the MLFF. This is the core part of the methodology. The MLFF is trained on the fly through MD calculations following the procedure outlined in ref. [28]. Two MLFF datasets were built: i) A light one on a 2×2×2 supercell with a 3×3×3 Γ-centered k-point mesh, and ii) a second one on a 3×3×3 supercell with a 2×2×2 Monkhorst-Pack k-point mesh. The MD runs were executed at increasing temperatures, sampling 50 000 steps at each temperature with a time step of 2 fs, and using the final structure at each temperature as the starting configuration for the higher ones. A Langevin thermostat was employed,[46] with a friction coefficient of 10 ps^{-1} for each atomic species.

ADVANCED
SCIENCE NEWS
www.advancedsciencenews.com

ADVANCED
QUANTUM
TECHNOLOGIES
www.advquantumtech.com

Figure 6. Sketch of the MLFF+SSCHA workflow. A first guess of the harmonic dynamical matrix is calculated at the DFT level or using the MLFF and employed by SSCHA in the generation of the first population (ensembles generation). The energies and forces for the displaced ensemble are computed employing the MLFF, and the gradient of the free energy is minimized in SSCHA (SSCHA matrix). The obtained SSCHA dynamical matrices are subsequently employed for the generation of the second population and the loop continues until convergence (arrow). After reaching convergence, the bubble correction at both static and dynamical level can be calculated.

For the descriptors representing the local atomic environments in the MLFF,[47] the cut-off radius for the two- and three-body atomic density distributions was set to 6 Å, and the Gaussian broadening to 0.3 Å. The same weight was assigned to both descriptors.

The 2×2×2 supercell dataset was used to train an MLFF to assess the accuracy of MLFF+SSCHA against direct DFT+SSCHA results obtained at 0 K on the same supercell size (Figure 3b). For this training, 225 structures were automatically extracted executing 3 MD simulations at 1, 100 and 200 K. The resulting root mean square errors (RMSE) for energies and forces for 100 random ensembles generated at 0 K using quantum statistics are 0.16 meV atom^{-1} and 0.020 eV Å^{-1}, respectively.

To achieve converged and accurate results at higher temperatures, we trained the second MLFF by sampling configurations up to 700 K in a larger 3×3×3 supercell. This is required in order to precisely compute the energies and forces related to the Gaussian distributed SSCHA ensembles up to room temperature. This dataset contains 680 reference configurations sampled by MD runs between 1 and 700 K, with steps of 100 K. A direct validation of MLFF+SSCHA was in this case not possible, since performing DFT+SSCHA on a 3×3×3 supercell turned out to be computationally prohibitive. To validate this MLFF, we computed the 1D and 2D energy landscape displayed in Figure 2a,b, showing excellent agreement with the DFT data. With this model, we obtained RMSEs very close to the ones obtained for the first (2×2×2) MLFF, 0.16 meV atom^{-1} and 0.027 eV Å^{-1}, for energies and forces, respectively, indicating a similar accuracy of both models. To guarantee a good performance of the MLFF up to 300 K, 100 ensembles were also generated at this temperature, and the associated RMSEs are 0.28 meV atom^{-1} and 0.056 eV Å^{-1}, slightly larger than those associated with 0 K ensembles.

4. Bubble correction and spectral function. The converged SSCHA matrix is finally corrected by the bubble self-energy term involving a three-phonon vertex, within the framework of a static Green's function approach where the free propagator is the one associated with the SSCHA Hamiltonian. The quartic SSCHA correction required to recover the full free energy curvature beyond the bubble term brought a negligible contribution to the soft mode at 0 and 300 K for both the 2×2×2 and 3×3×3 supercells. Therefore, one can conclude that the bubble term alone encodes virtually all relevant anharmonic effects taking place in KTO up to 300 K. To conduct a more robust comparison with measured phonon properties, we have computed the spectral function within a dynamical treatment that removes the conservation of energy and momentum in the multi-phonon processes.[27] An interpolation on a 13×13×13 k-mesh was employed in order to converge the peak positions.

4. Conclusions

In this work, we have illustrated that the inclusion of machine-learned force fields in the stochastic self-consistent harmonic approximation allows us to account for phonon properties of quantum paraelectric materials at finite-temperature, a property that is very difficult to access using standard first-principles approaches. For the incipient ferroelectric KTaO$_3$, this approach provides excellent predictions of higher-order anharmonic effects as a function of temperature, a key ingredient to characterize the unusual low-temperature behavior of this material. In particular, the peculiar temperature-dependent frequency plateau near 0 K is correctly reproduced capturing the essential features of the quantum paraelectric nature of KTaO$_3$.

The proposed ML-assisted method is capable to reproduce the Γ-point TO soft mode renormalization at 0 K with only 225 ab initio calculations, a small fraction of the thousands of calculations required in the standard SSCHA method. Adopting a larger MLFF training dataset of 680 structures sampled up to 700 K, the finite-temperature phonon properties were computed between 0 and 300 K. For each temperature point, several thousand conventional ab initio calculations would be required, an enormous computational effort compared to the few hundred required to produce an accurate MLFF.

Although MLFF+SSCHA provides a convincing qualitative trend for the phonons at finite-temperature, a quantitative account of the strongly temperature-dependent soft mode is still unattainable, including the recently reported minuscule upturn of the dielectric constant just above the absolute zero.[6] This would probably require the adaption of a more sophisticated exchange-correlation functional (beyond meta-GGA) and a careful treatment of (finite-temperature) volume effects: Both aspects will be the focus of future research.

Overall, the SSCHA+MLFF approach offers a convenient and flexible methodology for accessing complex anharmonicities as a function of temperature in real materials. The method enables to predict and interpret finite-temperature quantum effects extending the predictive power of computer modeling and providing essential support to experiment.

Supporting Information

Supporting Information is available from the Wiley Online Library or from the author.

Conflict of Interest

The authors declare no conflict of interest.

Data Availability Statement

The data that support the findings of this study are available from the corresponding author upon reasonable request.

[1] K. A. Müller, H. Burkard, *Phys. Rev. B* **1979**, *19*, 3593.

[2] R. A. Cowley, *Phys. Rev. Lett.* **1962**, *9*, 159.

[3] R. Migoni, H. Bilz, D. Bäuerle, *Phys. Rev. Lett.* **1976**, *37*, 1155.

[4] G. V. Belokopytov, *Ferroelectrics* **1995**, *168*, 69.

[5] F. Hideshi, K. Shou, S. Masahiro, I. Ryosuke, O. Hiroyuki, Y. Toshihisa, *J. Phys. Soc. Jpn.* **2016**, *85*, 74703.

[6] S. E. Rowley, L. J. Spalek, R. P. Smith, M. P. Dean, M. Itoh, J. F. Scott, G. G. Lonzarich, S. S. Saxena, *Nat. Phys.* **2014**, *10*, 367.

[7] S. Sachdev, *Quantum Phase Transitions*, Cambridge University Press, Cambridge **2000**.

[8] M. Tyunina, J. Narkilahti, M. Plekh, R. Oja, R. M. Nieminen, A. Dejneka, V. Trepakov, *Phys. Rev. Lett.* **2010**, *104*, 227601.

[9] G. A. Samara, *Phys. Rev.* **1966**, *151*, 378.

[10] H. Uwe, T. Sakudo, *Phys. Rev. B* **1976**, *13*, 271.

[11] M. Itoh, R. Wang, Y. Inaguma, T. Yamaguchi, Y.-J. Shan, T. Nakamura, *Phys. Rev. Lett.* **1999**, *82*, 3540.

[12] T. Esswein, N. A. Spaldin, *Phys. Rev. Research* **2022**, *4*, 033020.

[13] J. H. Barrett, *Phys. Rev.* **1952**, *86*, 118.

[14] W. Cochran, *Adv. Phys.* **1960**, *9*, 387.

[15] G. A. Samara, B. Morosin, *Phys. Rev. B* **1973**, *8*, 1256.

[16] R. P. Lowndes, A. Rastogi, *J. Phys. C: Solid State Phys.* **1973**, *6*, 932.

[17] C. H. Perry, R. Currat, H. Buhay, R. M. Migoni, W. G. Stirling, J. D. Axe, *Phys. Rev. B* **1989**, *39*, 8666.

[18] J. C. Slater, *Phys. Rev.* **1950**, *78*, 748.

[19] O. G. Vendik, *Sov. Phys. Solid State* **1972**, *14*, 849.

[20] A. B. Rechester, *Sov. Phys. JETP* **1971**, *33*, 423.

[21] D. E. Khmelnitskii, V. L. Shneerson, *Sov. Phys. JETP* **1973**, *37*, 164.

[22] R. Martoňák, E. Tosatti, *Phys. Rev. B* **1994**, *49*, 12596.

[23] W. Zhong, D. Vanderbilt, *Phys. Rev. B* **1996**, *53*, 5047.

[24] R. Martoňák, E. Tosatti, *Phys. Rev. B* **1996**, *54*, 15714.

[25] D. Shin, S. Latini, C. Schäfer, S. A. Sato, U. De Giovannini, H. Hübener, A. Rubio, *Phys. Rev. B* **2021**, *104*, L060103.

[26] D. Hooton, *Lond. Edinb. Dublin Philos. Mag. J. Sci.* **1955**, *46*, 422.

[27] L. Monacelli, R. Bianco, M. Cherubini, M. Calandra, I. Errea, F. Mauri, *J. Phys.: Condens. Matter* **2021**, *33*, 363001.

[28] R. Jinnouchi, F. Karsai, G. Kresse, *Phys. Rev. B* **2019**, *100*, 14105.

[29] O. Hellman, I. A. Abrikosov, S. I. Simak, *Phys. Rev. B: Condens. Matter Mater. Phys.* **2011**, *84*, 180301.

[30] I. Errea, M. Calandra, F. Mauri, *Phys. Rev. Lett.* **2013**, *111*, 177002.

[31] I. Errea, M. Calandra, F. Mauri, *Phys. Rev. B: Condens. Matter Mater. Phys.* **2014**, *89*, 064302.

[32] R. Bianco, I. Errea, L. Paulatto, M. Calandra, F. Mauri, *Phys. Rev. B* **2017**, *96*, 014111.

[33] L. Monacelli, I. Errea, M. Calandra, F. Mauri, *Phys. Rev. B* **2018**, *98*, 024106.

[34] Q. N. Meier, N. Mingo, A. van Roekeghem, arxiv.org/abs/2206.08296, **2022**.

[35] A. van Roekeghem, J. Carrete, N. Mingo, *Comput. Phys. Commun.* **2021**, *263*, 107945.

[36] J. Schmidt, M. R. G. Marques, S. Botti, M. A. L. Marques, *npj Comput. Mater.* **2019**, *5*, 83.

[37] V. L. Deringer, M. A. Caro, G. Csányi, *Adv. Mater.* **2019**, *31*, 1902765.

[38] O. T. Unke, S. Chmiela, H. E. Sauceda, M. Gastegger, I. Poltavsky, K. T. Schütt, A. Tkatchenko, K.-R. Müller, *Chem. Rev.* **2021**, *121*, 10142.

[39] H. Vogt, *Phys. Rev. B* **1995**, *51*, 8046.

[40] R. H. Lyddane, R. G. Sachs, E. Teller, *Phys. Rev.* **1941**, *59*, 673.

[41] G. Kresse, J. Hafner, *Phys. Rev. B* **1993**, *47*, 558.

[42] G. Kresse, J. Furthmüller, *Comput. Mater. Sci.* **1996**, *6*, 15.

[43] A. Togo, F. Oba, I. Tanaka, *Phys. Rev. B* **2008**, *78*, 134106.

[44] J. Sun, A. Ruzsinszky, J. Perdew, *Phys. Rev. Lett.* **2015**, *115*, 036402.

[45] G. Kresse, D. Joubert, *Phys. Rev. B* **1999**, *59*, 1758.

[46] W. G. Hoover, A. J. C. Ladd, B. Moran, *Phys. Rev. Lett.* **1982**, *48*, 1818.

[47] R. Jinnouchi, F. Karsai, C. Verdi, R. Asahi, G. Kresse, *J. Chem. Phys.* **2020**, *152*, 234102.